



An efficient micromixer combining oscillatory flow and divergent circular chambers

J. W. Wu¹ · H. M. Xia^{1,2} · Y. Y. Zhang¹ · S. F. Zhao³ · P. Zhu³ · Z. P. Wang⁴

Received: 3 August 2018 / Accepted: 15 October 2018 / Published online: 25 October 2018
© Springer-Verlag GmbH Germany, part of Springer Nature 2018

Abstract

Oscillatory/pulsatile flow is an important approach for mixing enhancement at micro scales. Here we report a micromixer that consists of a microfluidic oscillator and divergent chambers. The oscillator autonomously produces an oscillatory flow, which further causes efficient stretching and folding of the fluids to improve the mixing. Testing results show that the design works well at relatively high flow rates and high viscosities. At around 40 ml/min, the mixing index can reach 0.97 at 8 mPa s, and 0.89 at 12 mPa s, respectively. Efficient mixing can also be achieved at viscosity ratios of up to 10 (20 mPa s:2 mPa s). Application of the micromixer for preparation of nano sized RDX (cyclotrimethylenetrinitramine) is investigated. Using the anti-solvent crystallization method, nano-RDX particles with the size ranging from 150 to 900 nm are obtained. Its thermal decomposition characteristics are tested and compared with the raw RDX.

List of symbols

A	The pre-exponential factor (–)
D	Diffusion coefficient (m ² /s)
E_a	The apparent activation energy (kJ/mol)
f	Frequency of the oscillatory flow (Hz)
I_i	Pixel intensity (–)
I_{mix}	Pixel intensity after complete mixing (–)
I_{unmix}	Pixel intensity before mixing (–)
L	Characteristic length of fluid channel (mm)
P_o	Operating pressure of the microfluidic oscillator (bar)

Q	Flow rate (m ³ /s)
\bar{Q}_1	Time-averaged flow rate of the oscillatory flow applied at inlet 1 (ml/min)
Q_2	Flow rate at inlet 2 (ml/min)
R	Gas constant (J/(K mol))
Re	Reynolds number (–)
T	Oscillation period (s)
t	Time (s)
T_m	The temperature of molten endothermic peak (°C)
T_p	The temperature of thermal decomposition exothermic peak (°C)
U	Fluid velocity (m/s)

Electronic supplementary material The online version of this article (<https://doi.org/10.1007/s00542-018-4193-7>) contains supplementary material, which is available to authorized users.

✉ H. M. Xia
hmxia@njust.edu.cn

¹ School of Mechanical Engineering, Nanjing University of Science and Technology, Nanjing 210094, People's Republic of China

² Collaborative Innovation Center of High-end Equipment Manufacturing Technology, Nanjing University of Science and Technology, Nanjing 210094, People's Republic of China

³ School of Chemical Engineering, Nanjing University of Science and Technology, Nanjing 210094, People's Republic of China

⁴ Singapore Institute of Manufacturing Technology, 73 Nanyang drive, Singapore 637662, Singapore

Greek symbols

β	Heating rate (°C/min)
μ	Fluid viscosity (Pa s)
ν	Fluid kinematic viscosity (m ² /s)
σ	Mixing index (–)
τ	Normalized mixing time, $\tau = t/T$ (–)
χ	Viscosity ratio (–)

1 Introduction

Fluid mixing is an important topic in microreactor and microfluidic studies. It is involved in a variety of applications including biochemical analysis, medical diagnosis, and chemical synthesis (Kuo and Jiang 2014; Liu et al. 2003; Valencia et al. 2013; Wang et al. 2017b; Xia et al. 2015; Yang et al. 2015). However, in miniaturized fluid

devices the flow typically falls in the stable laminar regime due to increased viscous effects. Without turbulence, the fluid mixing mainly relies on the diffusion process, which is slow and may not meet relevant requirements (Squires and Quake 2005; Stone et al. 2004). To solve this problem, many micromixers including both the active and passive designs have been developed (Hessel et al. 2005; Nguyen 2011). Active micromixers work through pneumatic, magnetic, electrical, or acoustic actuations, and commonly require bulky external components. The energy input or heat transform may also destroy the biological samples (Lee et al. 2011; Zhang et al. 2011), limiting its applications. Passive micromixers (Chen et al. 2017; Hirata and Ohkawa 2016; Hossain and Kim 2015; Lin 2015; Stroock et al. 2002; Xia et al. 2018; Zhang et al. 2016) do not have moving parts, they utilize specially designed fluid channels to stir the fluids. But compared with the active design, its control is less flexible, the mixing performance depends more on the fluid properties and flow conditions.

Among the various microfluidic mixing methods, one important strategy is to apply oscillatory or pulsatile flows. Glasgow and Aubry (2003 and Glasgow et al. (2004) studied the fluid mixing using time pulsing of the incoming flow rates, and analyzed the influences of the Strouhal number, the pulse volume ratio, and the phase difference, etc. Cho et al. (2012) presented a novel crisscross micromixer by applying aperiodic time-varying electrokinetic perturbing flows, which is modulated in accordance with the oscillatory behavior of the Sprott system. Niu and Lee (2003), Niu et al. (2006) and Bottausci et al. (2007) proposed another micromixer design, for which the flow in a main channel was perturbed by oscillatory flows from orthogonal side channels to intensify the mixing. Tabeling et al. (2004) investigated the chaotic mixing in a cross-channel intersection under oscillatory flow conditions. Afzal and Kim (2015a, b) conducted numerical investigations on a convergent-divergent micromixer coupled with pulsatile flow and its optimization regarding the geometry and operating conditions.

However, most previous studies on oscillatory-flow micromixer have focused on the mixing at low kinematic viscosities (mostly $10^{-6} \text{ m}^2 \text{ s}^{-1}$) and low flow rates (in the range of $\sim \mu\text{l}/\text{min}$). Its performance for mixing high-viscosity fluids requires further exploration. As mentioned by Bottausci et al. (2007), complete mixing can be achieved only if the oscillations are strong enough to induce vortices. At high viscosities, it will be more difficult to impose effective perturbations to the fluids. On another aspect, the oscillatory mixing in a microchannel mainly attributes to the sequential fluid segmentation which shortens the axial mixing path (Nguyen and Huang 2005). But at a fixed frequency, a higher flow rate will generate longer fluid segments. It will reduce the contacting area between the

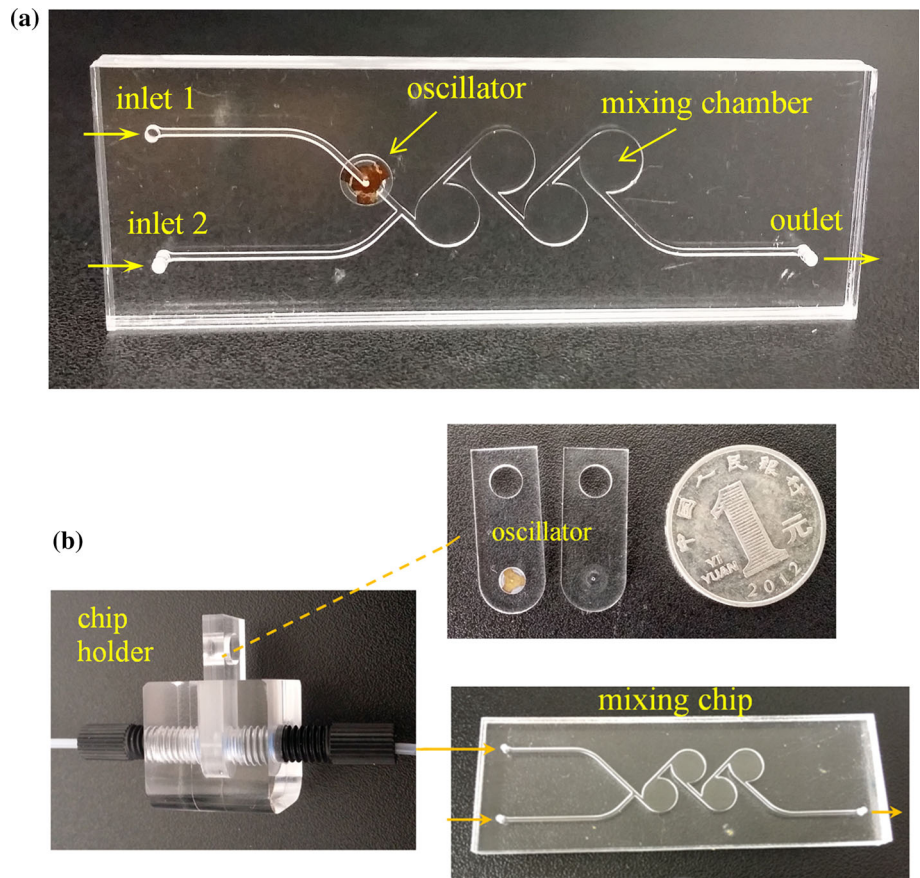
fluids and deteriorate the mixing. Another issue is that the pulsatile flow was usually generated by oscillating pumps or actively controlled actuators. It raises the operational complexity and contradicts the miniaturization requirements of $\mu\text{-TAS}$ and microreactor systems.

In this work, we propose a new oscillatory-flow micromixer for high-viscosity and high-flow-rate applications. The design is based on our previously developed negative-resistance microfluidic oscillator (Xia et al. 2012, 2017), which can autonomously convert a stable laminar flow to an oscillatory flow. It further combines circular chambers which intensify the mixing through fluid stretching and folding. Preparation of micro/nano energetic materials using current micromixer is demonstrated. As an example, nano-RDX is produced via an anti-solvent crystallization process, for which the mixing rate between the solution and anti-solvent is a key factor. As one important energetic material, nano-structured RDX exhibits some attractive features such as reduced sensitivity (Jung et al. 2016; Lee et al. 2014; Wang et al. 2017a). Here, the obtained product is compared with the raw material regarding the morphology, size distribution and thermal stability.

2 Micromixer design

Figure 1a is a photograph of current micromixer. It consists of two inlet channels, one outlet channel, and four mixing chambers. A microfluidic oscillator is embedded into one of the inlet channels. The oscillator has a small chamber that contains an elastic diaphragm, which is made of a spring metal (Copper/Beryllium (Cu98/Be2) foil, Goodfellow, UK). It works through a negative-differential-resistance mechanism. Driven by an incoming flow and above a critical pumping pressure, the diaphragm will produce self-excited oscillations, converting the flow into an oscillatory one. Though involving a moving part (i.e. the oscillating diaphragm), the pumping pressure remains constant during the operation so it works in a passive way without resorting to actively-controlled elements. The averaged flow rate (\bar{Q}) and oscillation frequency (f) are determined by its geometrical dimensions, bending stiffness of the diaphragm, the fluid viscosity and the operating pressure. For current design, depending on the applied fluid and operating pressure, the oscillation frequency (f) varies from around 120–220 Hz, and the averaged flow rate \bar{Q} varies from around 9–24 ml/min. In each oscillation period, the lowest flow rate is close to zero and the peak flow rate is around 2.5–3.5 times that of \bar{Q} . For more detailed information on this microfluidic oscillator, please refer to our previous reports (Xia et al. 2012, 2017).

Fig. 1 **a** A photograph of the current micromixer. The microfluidic oscillator is embedded into one of the inlet channels for producing oscillatory flow. **b** A more flexible plug-and-play design of the micromixer



As aforementioned, the oscillatory mixing in a microchannel relates to the applied flow rate. For the case where the two fluids to be mixed are alternately pumped into the main channel, at a fixed frequency, the length of fluid segments will increase with the flow rate, reducing the mixing efficiency. This was observed in our previous studies (Xia et al. 2015). To solve this problem, circular chambers are used in current design to extend the applicable flow rate range. The diameter and depth of the chamber are 5 mm and 0.5 mm, respectively. In currently tested flow rate and frequency range, the chamber volume is around 2-8 times that of the incoming fluids per cycle. The fluids flow into the chambers through a tangent microchannel of cross section 0.5 mm × 0.5 mm. At moderate Reynolds numbers ($Re = UL/v$, where U is the fluid velocity, L is the characteristic dimension of the channel, v is the kinematic viscosity of the fluid) when the fluid inertial plays a role, this configuration can induce micro-vortices for mixing enhancement (Alam and Kim 2013; Lin et al. 2005).

The mixer can also be designed in a plug-and-play manner. As shown in Fig. 1b, the oscillator works as an independent unit. It is connected to the mixing chip through a small chip-holder and sealing connectors with ferrules. In this way, it allows easy replacement of the

oscillator. The mixing chip is also simplified to a planar structure.

3 Experimental setup

3.1 Mixing test

To facilitate the mixing test, transparent PMMA material was chosen to fabricate the micromixer device. Conventional micro-milling and thermal bonding methods were employed. The applied liquid was glycerol-water mixture, whose viscosity is tunable through changing their volume ratio. To distinguish the two fluids to be mixed, black dye was added into one mixture. In experiments, the operating pressure (P_o) was applied to a pressurized liquid container (Nordson Corp.) to pump the liquid through the oscillator. P_o was controlled using a regulator and a digital pressure gauge (700G27, Fluke Corp., USA), but kept constant during the operation. The applied fluid was colorless and it was driven into inlet 1 of the mixer. The other fluid with black dye was introduced into inlet 2 using a syringe pump. The mixing pictures were recorded by a high-speed video camera (Photron FASTCAM Mini UX100) with a laptop.

The mixing efficiency was measured based on the pixel intensity. In this testing, there are two pixel intensities before mixing $I_{unmix,1}$ and $I_{unmix,2}$, corresponding to the liquids with and without black dye, respectively. Let I_{mix} stand for the pixel intensity of complete mixing, and I_i stand for the intermediate value during the mixing process. Suppose $I_{unmix,1} > I_{mix} > I_{unmix,2}$, a local deviation σ_i can be defined as

$$\sigma_i = \begin{cases} \frac{I_i - I_{mix}}{I_{unmix,1} - I_{mix}} & (if I_{unmix,1} \geq I_i > I_{mix}) \\ \frac{I_i - I_{mix}}{I_{unmix,2} - I_{mix}} & (if I_{mix} > I_i \geq I_{unmix,2}) \end{cases} \quad (1)$$

Then, the mixing degree is calculated as

$$\sigma = 1 - \sqrt{\frac{\sum_{i=1}^N (\sigma_i)^2}{N}} \quad (2)$$

The value of σ ranges from 0 for non-mixing to 1 for complete mixing. More information on similar fabrication and testing methods of a micromixer can be found in Xia et al. (2018).

3.2 Preparation of nano-RDX

To prepare nano-RDX, dimethyl sulfoxide (DMSO, Sino-pharm, China) was chosen as the solvent, deionized water (DI water) was used as the anti-solvent, and the oscillation was applied to the latter. The raw RDX was obtained from Yinguang Chemical (Gansu, China). Its concentration in DMSO was 0.04 g/ml. To reduce the particle agglomeration, 0.1 w% of hexadecyltrimethylammonium chloride (CTAC, Usolf, China) was dissolved in the deionized water as a stabilizer.

Immediately after the recrystallization process, around 0.1 ml nano-RDX suspension was diluted 1000 times for SEM (scanning electron microscope) measurement. The rest solution was collected for PSD (particle size distribution) and DSC (differential scanning calorimeter) test. All the suspension was freeze-dried with a freeze dryer (BIOBASE, China).

4 Mixing results and discussion

4.1 Mixing in steady flow vs. oscillatory mixing

Figure 2 compares the experimental mixing results with and without oscillatory flow at dynamic viscosity $\mu = 8$ mPa s. For the steady flow, $Q_1 = Q_2 = 22$ ml/min, the corresponding Re is ~ 183 . Figure (a) shows that, at this Re the circular chambers cannot induce micro-vortices. Though swirling flows do occur as observed in the second

and fourth chambers, they are too weak to cause a substantial enhancement of the mixing. The two fluids basically keep separated, after four mixer units the mixing index σ only reaches 0.23. In comparison, the oscillatory mixing as shown in figure (b) is much more efficient. In this test, the operating pressure of the oscillator P_o is 6.3 bar, producing an oscillatory flow of 119 Hz. At a same flow rate, $\bar{Q}_1 = \bar{Q}_2 = 22$ ml/min, the mixing is clearly intensified through fluid perturbations. The mixture has become rather homogeneous (please see the supplementary video 1).

The mixing results during one cycle in the first chamber are displayed in Fig. 3. In the first 1.2 ms, the microchannel is full of fluid 2 (the black one). Then, the flow rate of fluid 1 (the colorless one) (Q_1) gradually increases, squeezing fluid 2 into a thin stream layer. After around 7.2 ms, Q_1 decreases and fluid 2 occupies the microchannel again. The periodic variation in Q_1 has caused strong stirring effects. As a result, the flow becomes rather chaotic leading to more efficient mixing.

Figure 4 plots the quantified mixing results in all the four chambers. It shows that the mixing index σ exhibits large variations during one oscillation period in the first chamber. It varies from 0.70 to 0.77 due to the pulsating flow rate. After that, σ becomes rather constant. It quickly increases to 0.84 and 0.92 in the second and third chamber, and finally reaches 0.97 in the fourth chamber, suggesting that the fluids are fully mixed.

4.2 Influence of operating pressure and fluid viscosity

Figure 5 compares the mixing results at 12 mPa s under different operating pressures of the oscillator. It is found that, when P_o is increased from 5.5 bar to 6.5 bar, the mixing becomes better and σ is improved from 0.81 to 0.89 in the fourth chamber (see Fig. 6). This can be explained by the working characteristics of the microfluidic oscillator. According to our previous studies (Xia et al. 2012), the oscillation frequency f increases and the flow rate \bar{Q} decreases with P_o . For the current case, when P_o is increased from 5.5 to 6.5 bar, f increased from 131 to 217 Hz while \bar{Q} drops from 16.5 to 13.5 ml/min. Accordingly, in the latter case it forms more fluid laminations, as can be seen from the first chamber. The enlarged fluid interface facilitates the diffusive mixing.

To explore the applicable viscosity range of current mixer, the mixing at different viscosities was examined and relevant results are presented in Fig. 6. As can be expected, the mixing efficiency decreases with the fluid viscosity. At $\mu = 1$ mPa s, the mixing result is slightly better than that at $\mu = 8$ mPa s, and σ is around 0.98. When μ is increased to

Fig. 2 Experimental mixing results in the four circular chambers at $\mu = 8 \text{ mPa s}$ (the flow direction is from left to right). **a** Mixing in a steady flow, $Q_1 = Q_2 = 22 \text{ ml/min}$. **b** Snapshot of oscillatory mixing, $\bar{Q}_1 = \bar{Q}_2 = 22 \text{ ml/min}$

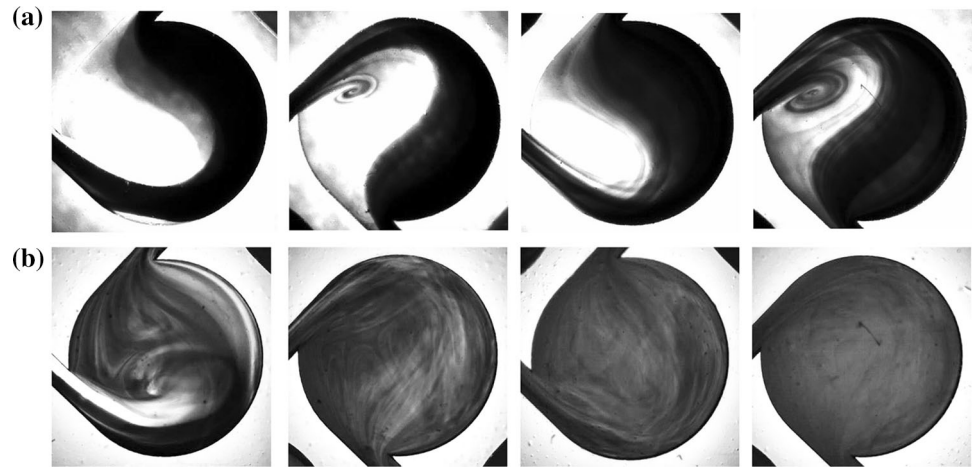


Fig. 3 Snapshots of the mixing during one oscillation period in the first chamber at $\mu = 8 \text{ mPa s}$

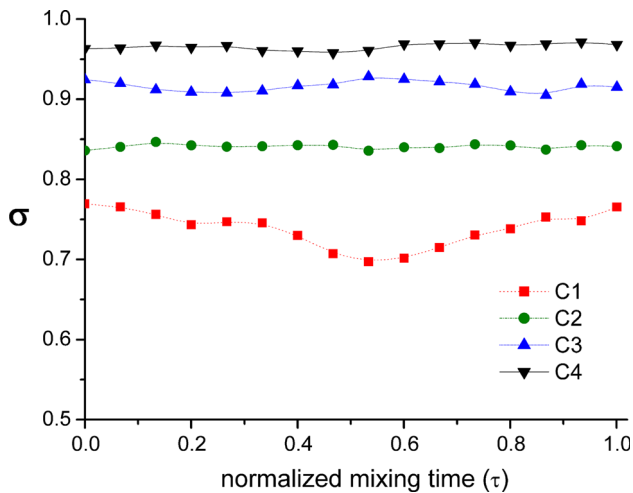
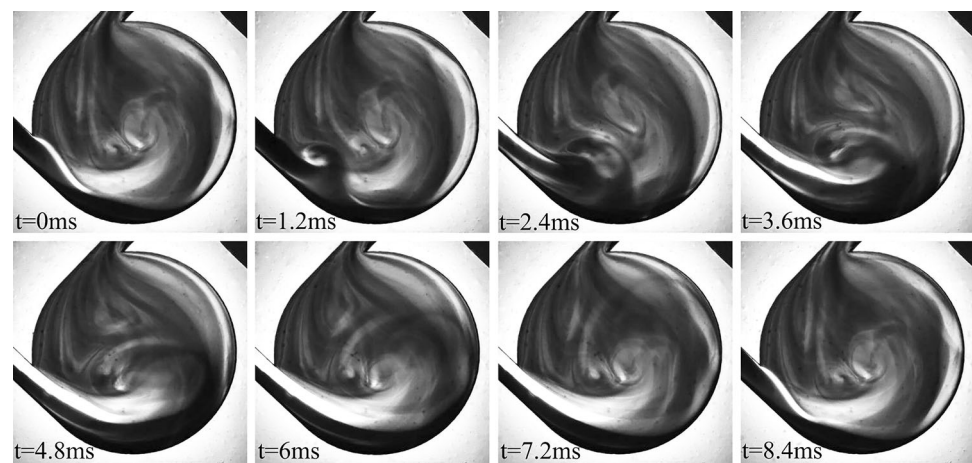


Fig. 4 The change of σ over the normalized mixing time τ at $\mu = 8 \text{ mPa s}$ ($\tau = t/T$, where T is the oscillation period). $\bar{Q}_1 = \bar{Q}_2 = 22 \text{ ml/min}$. C1–C4 indicate the 1st–4th mixing chambers

12 mPa s, the mixing becomes slower and incomplete, σ only reaches 0.89 at $P_o = 6.5 \text{ bar}$. This is because the flow

is more stable and the diffusion also becomes weaker at high viscosities.

4.3 Mixing at different flow rate and viscosity ratios

More testing was conducted at $\mu = 16 \text{ mPa s}$ and 20 mPa s at flow rate ratio $\bar{Q}_1:\bar{Q}_2 = 4:1$. As shown in Fig. 7, under this condition, the fluid distribution patterns can be clearly captured. At 20 mPa s , when fluid 2 (the black one) enters the circular chamber, it is stretched by the rotating flow. Then, under oscillatory perturbations from fluid 1, it forms fine multiple laminations. At 16 mPa s , the fluid structure becomes less regular. Besides stretching, folding of the fluid interfaces is also observed. This is because as the fluid viscosity is reduced, the increased inertial effects enable the fluids to move a longer distance along the circumferential direction. Then, as they flow towards the outlet channel, the fluid interfaces are folded up in the convergent region (please see the supplementary video 2 for more details).

Fig. 5 Snapshots of the oscillatory mixing at $\mu = 12 \text{ mPa s}$ in the four mixing chambers. **a** The operating pressure of the oscillator, $P_0 = 5.5 \text{ bar}$, the corresponding frequency, $f = 131 \text{ Hz}$, $\bar{Q}_1 = \bar{Q}_2 = 16.5 \text{ ml/min}$. **b** $P_0 = 6.5 \text{ bar}$, $f = 217 \text{ Hz}$, $\bar{Q}_1 = \bar{Q}_2 = 13.5 \text{ ml/min}$

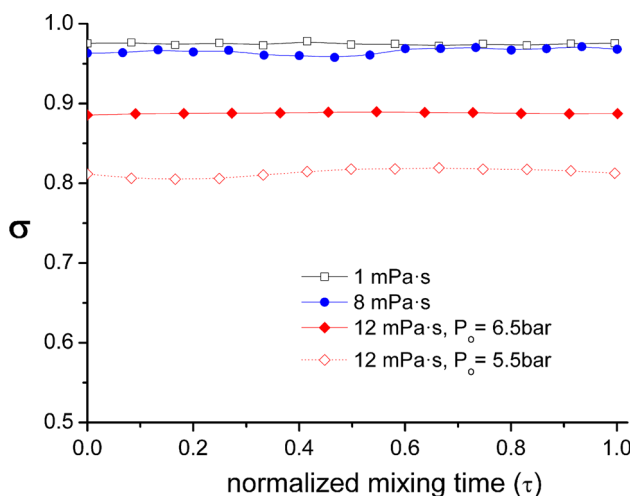
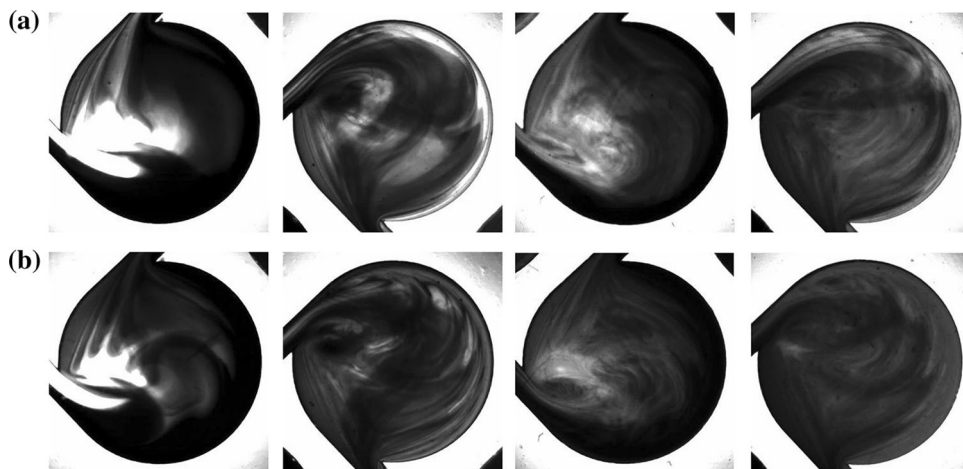


Fig. 6 The mixing in the fourth chamber versus the normalized mixing time at different viscosities and P_0 . The flow rates are as follows. At 1 mPa s : $\bar{Q}_1 = \bar{Q}_2 = 24.0 \text{ ml/min}$; at 8 mPa s : $\bar{Q}_1 = \bar{Q}_2 = 22 \text{ ml/min}$; at 12 mPa s , 6.5 bar : $\bar{Q}_1 = \bar{Q}_2 = 13.5 \text{ ml/min}$; at 12 mPa s , 5.5 bar : $\bar{Q}_1 = \bar{Q}_2 = 16.5 \text{ ml/min}$

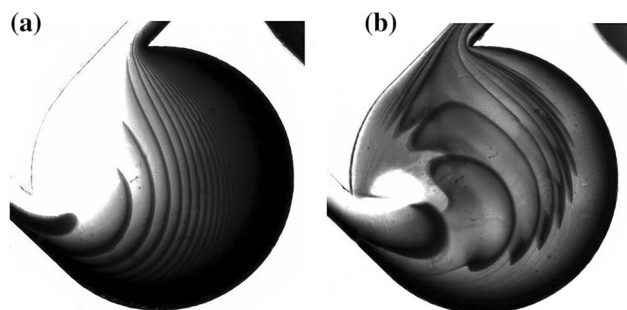


Fig. 7 Fluid distribution patterns in the 1st chamber at different viscosities. For both the cases, the flow rate ratio is $\bar{Q}_1:Q_2 = 4:1$, the operating pressure $P_0 \sim 5.5 \text{ bar}$. **a** $\mu = 20 \text{ mPa s}$, $\bar{Q}_1 = 9.2 \text{ ml/min}$, $Q_2 = 2.3 \text{ ml/min}$, **b** $\mu = 16 \text{ mPa s}$, $\bar{Q}_1 = 15.6 \text{ ml/min}$, $Q_2 = 3.9 \text{ ml/min}$

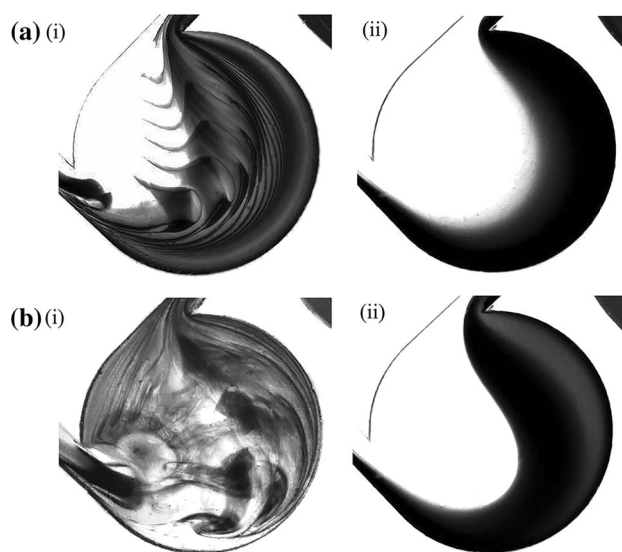


Fig. 8 Fluid distribution patterns in the 1st chamber with (i) and without (ii) oscillatory flow at different viscosity ratios, $\bar{Q}_1:Q_2 = 4:1$, $P_0 \sim 5.5 \text{ bar}$. **a** $\mu_1:\mu_2 = 20\text{mPa s}:2\text{mPa s}$, $\bar{Q}_1(Q_1) = 9.1 \text{ ml/min}$, $Q_2 = 2.3\text{ml/min}$, **b** $\mu_1:\mu_2 = 16\text{mPa s}:2\text{mPa s}$, $\bar{Q}_1(Q_1) = 15.2 \text{ ml/min}$, $Q_2 = 3.8\text{ml/min}$

Figure 8 presents the results at different viscosity ratios (χ). For the case of $\mu_1:\mu_2 = 20\text{mPa s}:2\text{mPa s}$ ($\chi = 10$), the fluid viscosity continuously changes through mixing (μ will become 10.7 mPa s after complete mixing). Compared with the mixing at $\mu_1 = \mu_2 = 20 \text{ mPa s}$ (see Fig. 7a), the flow becomes rather irregular. As shown in figure (a.i), besides the stretching and folding, some of the low-viscosity fluid (the black one) also penetrates into the higher-viscosity fluid (the colorless one), forming thin fluid threads. Figure 8(b.i), shows the results at $\mu_1:\mu_2 = 16\text{mPa s}:2\text{mPa s}$ ($\chi = 8$). In this case the flow becomes very chaotic, no clear fluid patterns can be identified. In comparison, for both the case without oscillatory perturbations, the flow remains very stable and the mixing is poor.

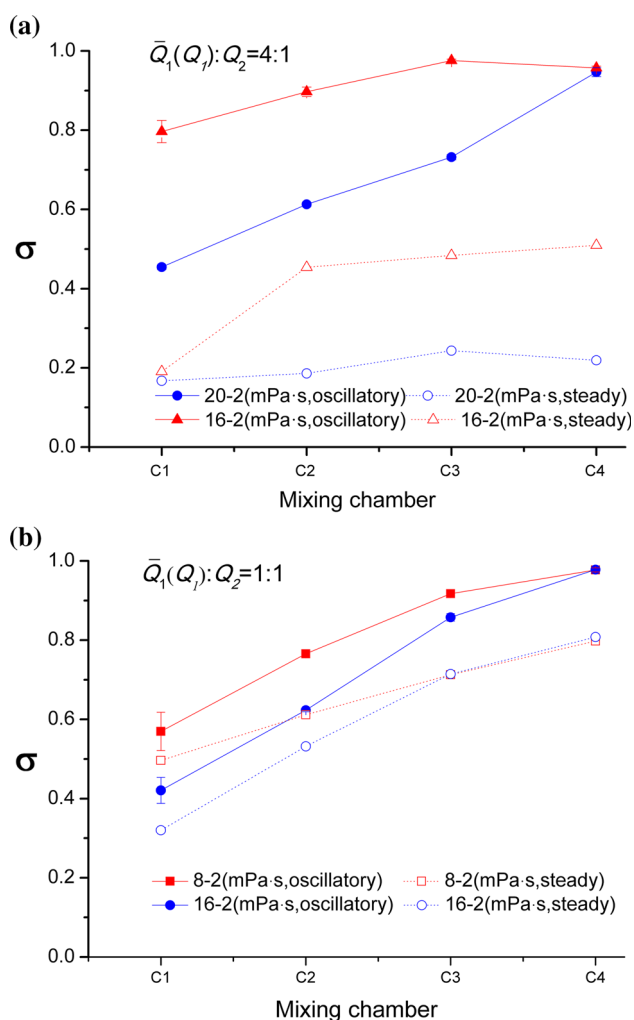


Fig. 9 Quantified mixing results at different viscosity ratios. **a** $\bar{Q}_1(Q_1):Q_2 = 4:1$. The specific flow rates are as given in the caption of Fig. 8. **b** $\bar{Q}_1(Q_1) = Q_2$. For the case of $\mu_1:\mu_2 = 8 \text{ mPa s}:2 \text{ mPa s}$, $P_o = 6.1 \text{ bar}$, $\bar{Q}_1(Q_1) = Q_2 = 19.2 \text{ ml/min}$. For the case of $\mu_1:\mu_2 = 16 \text{ mPa s}:2 \text{ mPa s}$, $P_o = 5.9 \text{ bar}$, $\bar{Q}_1(Q_1) = Q_2 = 13.0 \text{ ml/min}$

Figure 9a plots the quantified mixing results at different χ and at flow rate ratio $\bar{Q}_1:Q_2 = 4:1$. Without oscillatory flow, the mixing index σ only reaches 0.22 and 0.51 after four chambers for the case of $\mu_1:\mu_2 = 20 \text{ mPa s}:2 \text{ mPa s}$ and $\mu_1:\mu_2 = 16 \text{ mPa s}:2 \text{ mPa s}$, respectively. With oscillatory flow, the mixing is much faster and σ can reach around 0.95. Figure 9b presents the results at $\bar{Q}_1 = Q_2$. For the case of $\mu_1:\mu_2 = 16 \text{ mPa s}:2 \text{ mPa s}$, the mixing index σ is only 0.42 in the first chamber. But as the flow rate of the low-viscosity fluid (Q_2) is increased, σ increases rapidly in the subsequent chambers. It finally reaches 0.99, indicating a very good mixing. When the fluid viscosity is reduced to $\mu_1:\mu_2 = 8 \text{ mPa s}:2 \text{ mPa s}$, the mixing is further improved. For both the case without oscillatory flow, the mixing is

much slower and σ is less than 0.8 in the fourth mixing chamber.

5 Application for preparation of nano-RDX

Nano-RDX was prepared using current micromixer through the anti-solvent crystallization method. Conventionally, this process was performed in a batch mode using a mixing vessel. The mixing efficiency of the solution and anti-solvent usually plays an important role. It influences the nucleation stage, and determines the particle size distribution and the morphology uniformity. Using a micromixer, the process can be carried out in a continuous mode. The enhanced mixing is also supposed to improve the quality of the final product.

In current study, the flow rate ratio of anti-solvent to RDX solution was fixed at 15:1, and the flow rate of DI water was fixed at 16.6 ml/min. Figure 10 compares the SEM images of raw RDX and nano-RDX produced using the

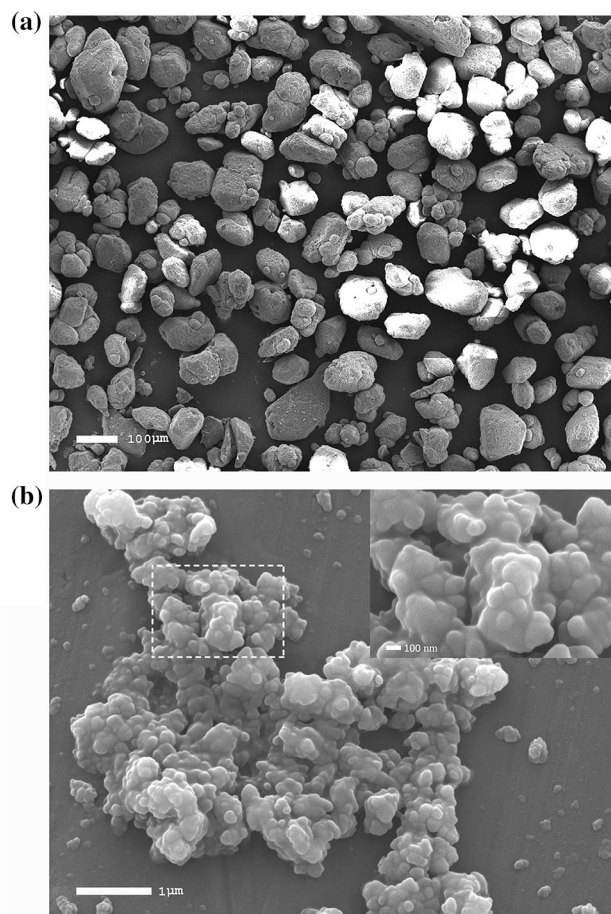


Fig. 10 SEM images of RDX particles. **a** Raw RDX material with an average size about 60 μm . **b** Recrystallized RDX particles. The flow rate ratio $\bar{Q}_1(\text{water}):\bar{Q}_2(\text{DMSO}) = 15:1$ (16.6 ml/min:1.1 ml/min), the concentration of RDX in DMSO is 0.04 g/ml

oscillatory micromixer. From figure (a), the size of raw RDX particles ranged from 30 to 70 μm , with a large variation. Defects on the crystal surface can be observed. Figure (b) presents the morphology of nano-RDX. Though the RDX particles intend to agglomerate, the size of individual RDX particle is in the level of several hundred nanometers. It is also found that these particles are somewhat amorphous with smooth surfaces. This is believed due to the rapid mixing and precipitation process. Upon mixing with the anti-solvent the RDX solution immediately reaches the over-saturation state, the precipitated RDX may not have enough time to form highly-structured crystals. Instead, the produced nano-RDX particles exhibit amorphous structures.

The corresponding particle size distribution (PSD) results of raw and refined RDX are shown in Fig. 11. For raw RDX, the particles are highly polydisperse with the size varying from around 20–120 μm . After recrystallization, the size of RDX particles is greatly reduced, and the whole size distribution becomes much narrower. Most particles are in the range of 200–400 nm with an average size of about 290 nm. Compared with the SEM photos, the

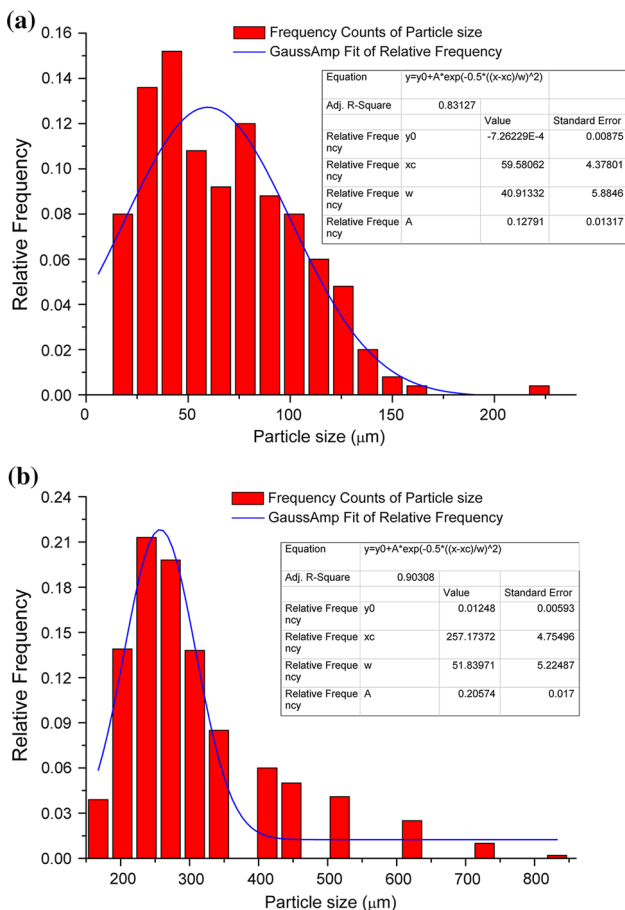


Fig. 11 Particle size distribution of **a** raw RDX and **b** recrystallized nano-RDX

size is a little larger and it is probably caused by agglomeration.

To examine the thermal decomposition characteristic of the RDX particles, thermogravimetric analysis (TGA) and differential scanning calorimeter (DSC) method are applied. During the testing process, nitrogen serves as the shielding gas. The heating rate (β) is set at 5 $^{\circ}\text{C}/\text{min}$ and the heating temperature ranges from 50 to 350 $^{\circ}\text{C}$. Figure 12 plots the thermal weightlessness process of RDX. For nano-RDX, the starting decomposition temperature is 138.4 $^{\circ}\text{C}$, and the termination temperature is 238.0 $^{\circ}\text{C}$. They are 4.8 $^{\circ}\text{C}$ and 0.7 $^{\circ}\text{C}$ lower than that of raw RDX, respectively. The DTG peak temperature of nano-RDX is 225.7 $^{\circ}\text{C}$, which is also 2.3 $^{\circ}\text{C}$ lower than that of raw RDX.

Figure 13 presents the DSC curves of raw RDX and nano-RDX at different heating rates. Both the RDX particles experience the process of melting and thermal decomposition with the increase of temperature. At the same heating rate, the temperatures of molten endothermic

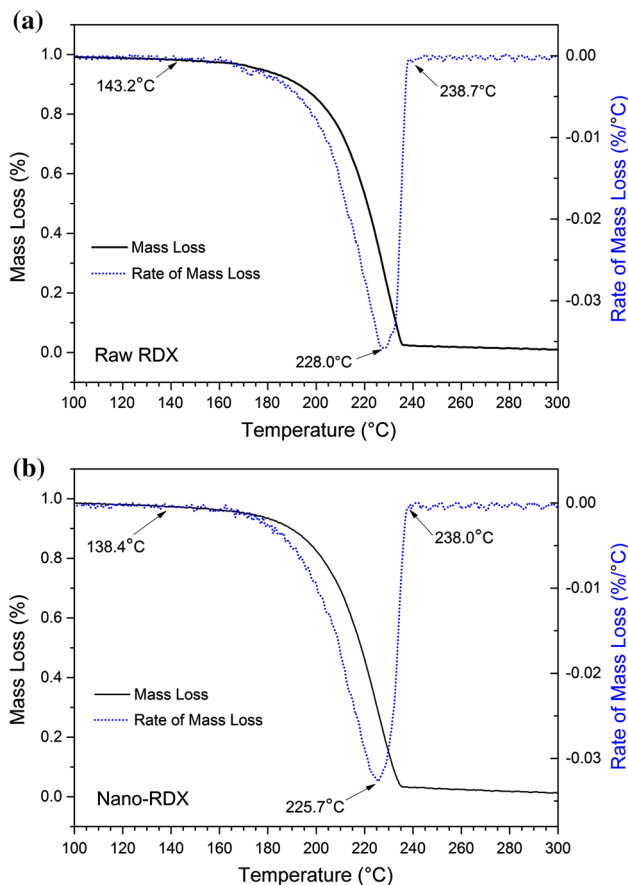


Fig. 12 TG and DTG curves of **a** raw RDX and **b** nano-RDX. The heating rate is 5 $^{\circ}\text{C}/\text{min}$. The starting decomposition temperature and termination temperature of raw RDX are 143.2 $^{\circ}\text{C}$ and 238.7 $^{\circ}\text{C}$. For nano-RDX, they are reduced to 138.4 $^{\circ}\text{C}$ and 238.0 $^{\circ}\text{C}$. The DTG peak temperature for raw RDX and nano-RDX are 228.0 $^{\circ}\text{C}$ and 225.7 $^{\circ}\text{C}$, respectively

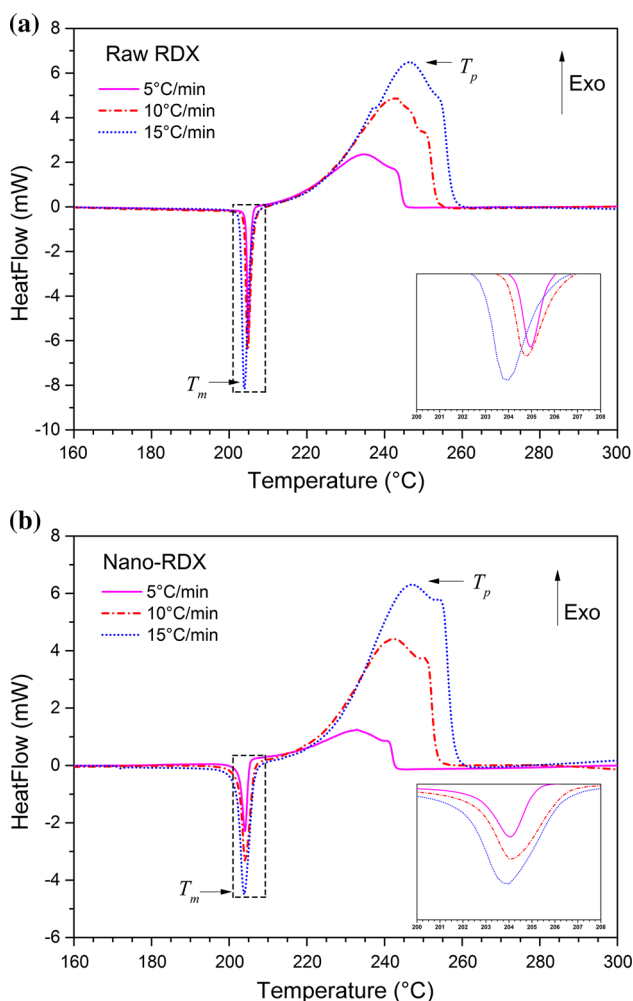


Fig. 13 DSC curves of **a** raw RDX and **b** nano-RDX. At different heating rates of 5 °C/min, 10 °C/min, 15 °C/min, the temperatures of molten endothermic peak (T_m) of raw RDX are 205 °C, 204.8 °C, 204 °C, and the thermal decomposition exothermic peak (T_p) are 234.7 °C, 242.8 °C, 247.2 °C, respectively. For nano-RDX, T_m = 204.1 °C, 204 °C, 203.9 °C, T_p = 233 °C, 242.2 °C, 246.7 °C, respectively

peak (T_m) and thermal decomposition exothermic peak (T_p) of nano RDX particles are a little lower than raw RDX particles. At 5 °C/min, the T_m of nano-RDX is 204.1 °C, which is 0.9 °C lower than that of raw RDX (i.e., $\Delta T_m = -0.9$ °C). For T_p , it is 233 °C, 1.7 °C lower than that of raw RDX (i.e., $\Delta T_p = -1.7$ °C). At 10 °C/min, $\Delta T_m = -0.8$ °C, $\Delta T_p = -0.6$ °C; at 15 °C/min, $\Delta T_m = -0.1$ °C, $\Delta T_p = -0.5$ °C. Results also show that for both the raw and nano-RDX, T_p increases with the heating rate. As aforementioned the nano-RDX particles are somewhat amorphous, and hence thermally less stable than raw RDX particles. This explains the reduction in the starting decomposition and termination temperatures of nano-RDX and the shifting of its DTG and DSC curves towards the lower temperature.

According to Kissinger method ($\ln((\beta)/T_p^2) = \ln(AR/E_a) - E_a/RT_p$, where R is gas constant and it is 8.314 J/(K mol)), the apparent activation energy E_a and pre-exponential factor A of thermal decomposition and exothermic reaction can be obtained. Figure 14 presents the linear fitting plot, both R-square are larger than 0.99. E_a of nano-RDX is 165.1 kJ/mol, which is 18.6 kJ/mol (or 10.1%) lower than that of raw RDX. The pre-exponential factor A of nano-RDX is 4.1×10^{16} while for raw RDX it is 3.3×10^{18} .

6 Conclusions

An efficient micromixer is developed consisting of a microfluidic oscillator and divergent circular chambers. The oscillator produces self-excited oscillations to enhance the mixing, reducing the reliance on external electrical components. So it combines the advantages of both the passive and active designs. The circular chambers solve the problem of formation of long fluid segments in microchannels, making it a more efficient design for high flow rate applications. The micromixer is applicable for high-viscosity fluids. Results show that at $\mu = 8$ mPa s and a total flow rate of $Q_t = 44$ ml/min, the mixing index σ can reach 0.97 after four mixer units. At $\mu = 12$ mPa s and $Q_t \sim 27$ ml/min, σ can reach 0.89. The design also works well for mixing fluids of largely different viscosities. All these abilities make it a robust and more universal device.

As an example, application of the micromixer for preparation of nano-RDX was demonstrated. Using the anti-solvent crystallization method, nano-RDX particles can be produced. The refined RDX has a much narrower PSD, and the average size is around 290 nm. DSC tests show that, compared to raw RDX, the temperature of

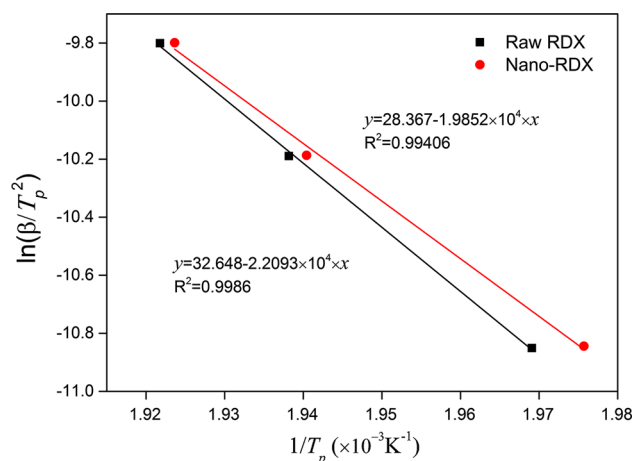


Fig. 14 Kissinger's plot of raw RDX and nano-RDX. Both the R-square are larger than 0.99

thermal decomposition exothermic peak of nano-RDX is reduced by 1.7 °C, 0.6 °C and 0.5 °C at heating rate of 5 °C/min, 10 °C/min and 15 °C/min, respectively. The apparent activation energy E_a of nano-RDX is 18.6 kJ/mol lower than that of raw RDX. Successful preparation of nano-RDX proves that this micromixer can be used as a research tool for screening the optimal parameters for chemical synthesis.

Acknowledgements This work was supported in part by the National Natural Science Foundation of China (51575282), the Fundamental Research Funds for the Central Universities (30915118803; 30916012101), the Priority Academic Program Development of Jiangsu Higher Education Institutions.

References

- Afzal A, Kim KY (2015a) Convergent-divergent micromixer coupled with pulsatile flow. *Sensor Actuat B-Chem* 211:198–205
- Afzal A, Kim KY (2015b) Optimization of pulsatile flow and geometry of a convergent-divergent micromixer. *Chem Eng J* 281:134–143
- Alam A, Kim KY (2013) Mixing performance of a planar micromixer with circular chambers and crossing constriction channels. *Sensor Actuat B-Chem* 176:639–652
- Bottausci F, Cardonne C, Meinhart C, Mezić I (2007) An ultrashort mixing length micromixer: The shear superposition micromixer. *Lab Chip* 7(3):396–398
- Chen XY, Li TC, Hu ZL (2017) A novel research on serpentine microchannels of passive micromixers. *Microsyst Technol* 23(7):2649–2656
- Cho CC, Chen CL, Chen CK (2012) Mixing enhancement in crisscross micromixer using aperiodic electrokinetic perturbing flows. *Int J Heat Mass Tran* 55(11–12):2926–2933
- Glasgow I, Aubry N (2003) Enhancement of microfluidic mixing using time pulsing. *Lab Chip* 3(2):114–120
- Glasgow I, Lieber S, Aubry N (2004) Parameters influencing pulsed flow mixing in microchannels. *Anal Chem* 76(16):4825–4832
- Hessel V, Löwe H, Schönfeld F (2005) Micromixers—a review on passive and active mixing principles. *Chem Eng Sci* 60(8–9):2479–2501
- Hirata Y, Ohkawa K (2016) Development of channel mixers utilizing 180° fluid rotation combined with split and recombination. *Chem Eng Res Des* 108:118–125
- Hossain S, Kim KY (2015) Mixing analysis in a three-dimensional serpentine split-and-recombine micromixer. *Chem Eng Res Des* 100:95–103
- Jung W, Park J, Lee W, Lee J, Koo K, Oh M (2016) Scale-up of a crystallizer for production of nano-sized energetic materials. *Chem Eng Technol* 39(7):1309–1316
- Kuo JN, Jiang LR (2014) Design optimization of micromixer with square-wave microchannel on compact disk microfluidic platform. *Microsyst Technol* 20(1):91–99
- Lee CY, Chang CL, Wang YN, Fu LM (2011) Microfluidic mixing: a review. *Int J Mol Sci* 12(5):3263–3287
- Lee JE, Kim JW, Han SK, Chae JS, Lee KD, Koo KK (2014) Production of submicrometer-sized hexahydro-1,3,5-trinitro-1,3,5-triazine by drowning-out. *Ind Eng Chem Res* 53(12):4739–4747
- Lin Y (2015) Numerical characterization of simple three-dimensional chaotic micromixers. *Chem Eng J* 277:303–311
- Lin CH, Tsai CH, Fu LM (2005) A rapid three-dimensional vortex micromixer utilizing self-rotation effects under low Reynolds number conditions. *J Micromech Microeng* 15(5):935–943
- Liu RH, Lenigk R, Druyor-Sanchez RL, Yang JN, Grodzinski P (2003) Hybridization enhancement using cavitation microstreaming. *Anal Chem* 75(8):1911–1917
- Nguyen NT (2011) *Micromixers: fundamentals, design and fabrication*. William Andrew Norwich, New York, p 2011
- Nguyen NT, Huang XY (2005) Mixing in microchannels based on hydrodynamic focusing and time-interleaved segmentation: modelling and experiment. *Lab Chip* 5(11):1320–1326
- Niu XZ, Lee YK (2003) Efficient spatial-temporal chaotic mixing in microchannels. *J Micromech Microeng* 13(3):454–462
- Niu XZ, Liu LY, Wen WJ, Sheng P (2006) Active microfluidic mixer chip. *Appl Phys Lett* 88(15)
- Squires TM, Quake SR (2005) Microfluidics: fluid physics at the nanoliter scale. *Rev Mod Phys* 77(3):977–1026
- Stone HA, Stroock AD, Ajdari A (2004) Engineering flows in small devices: Microfluidics toward a lab-on-a-chip. *Annu Rev Fluid Mech* 36:381–411
- Stroock AD, Dertinger SKW, Ajdari A, Mezić I, Stone HA, Whitesides GM (2002) Chaotic mixer for microchannels. *Science* 295(5555):647–651
- Tabeling P, Chabert M, Dodge A, Jullien C, Okkels F (2004) Chaotic mixing in cross-channel micromixers. *Philos T Roy Soc A* 362(1818):987–1000
- Valencia PM, Pridgen EM, Rhee M, Langer R, Farokhzad OC, Karnik R (2013) Microfluidic platform for combinatorial synthesis and optimization of targeted nanoparticles for cancer therapy. *ACS Nano* 7(12):10671–10680
- Wang BB, Liao X, Wang ZS, DeLuca LT, Liu ZT, Fu Y (2017a) Preparation and properties of a nRDX-based propellant. *Propell Explos Pyrot* 42(6):649–658
- Wang JC, Zhang F, Wang YJ, Luo GS (2017b) Preparation of In(OH)(3) Nanorods and nanocubes and the effect on In2O3 particle size in the microreactor. *Ind Eng Chem Res* 56(23):6637–6644
- Xia HM, Wang ZP, Fan W, Wijaya A, Wang W, Wang ZF (2012) Converting steady laminar flow to oscillatory flow through a hydroelasticity approach at microscales. *Lab Chip* 12(1):60–64
- Xia HM, Seah YP, Liu YC, Wang W, Toh AGG, Wang ZP (2015) Anti-solvent precipitation of solid lipid nanoparticles using a microfluidic oscillator mixer. *Microfluid Nanofluid* 19(2):283–290
- Xia HM, Wu JW, Wang ZP (2017) The negative-differential-resistance (NDR) mechanism of a hydroelastic microfluidic oscillator. *J Micromech Microeng* 27(7):075001
- Xia HM, Wu JW, Wang ZP (2018) A comparative discussion of different designs of passive micromixers: specific sensitivities of mixing efficiency on Reynolds numbers and fluid properties. *Microsyst Technol* 24(2):1253–1263
- Yang AS, Chuang FC, Chen CK, Lee MH, Chen SW, Su TL, Yang YC (2015) A high-performance micromixer using three-dimensional Tesla structures for bio-applications. *Chem Eng J* 263:444–451
- Zhang K, Guo SS, Zhao LB, Zhao XZ, Chan HLW, Wang Y (2011) Realization of planar mixing by chaotic velocity in microfluidics. *Microelectron Eng* 88(6):959–963
- Zhang WP, Wang X, Feng X, Yang C, Mao ZS (2016) Investigation of mixing performance in passive micromixers. *Ind Eng Chem Res* 55(38):10036–10043

Publisher's Note Springer Nature remains neutral with regard to jurisdictional claims in published maps and institutional affiliations.